Journal of Structural Geology 102 (2017) 193–207

Contents lists available at ScienceDirect

Journal of Structural Geology

journal homepage: www.elsevier.com/locate/jsg

Stress concentrations around voids in three dimensions: The roots of failure

T. Davis [a, b, *], D. Healy [a], A. Bubeck [c], R. Walker [c]

[a] School of Geosciences, King's College, University of Aberdeen, Aberdeen, AB24 3UE, UK
[b] GFZ German Research Centre for Geosciences, Telegrafenberg, 14473 Potsdam, Germany
[c] Department of Geology, University of Leicester, Leicester, UK

ARTICLE INFO

Article history:
Received 7 April 2017
Received in revised form
3 July 2017
Accepted 30 July 2017
Available online 3 August 2017

Keywords:
Stress
Concentrations
Voids
3D
Failure
Porosity

ABSTRACT

We present stress concentration factors at the edges of 3D voids in uniaxial compression. Variations in these stress concentration factors due to Poisson's ratio of the host material, void shape, and void-void proximity are explicitly quantified. Voids loaded by a vertical compressive stress are hypothesised to fail in one or two ways: (1) tension crack development due to tensile stress concentrations at the void poles; or (2) compressive stress concentrations at the void sides causing the void wall to fail in shear. The stress concentration factors in this study are found using the numerical displacement discontinuity method. Equations are provided to assess the proximity of a void to the two hypothesised modes of failure. For 3D voids thinned in an axis that lies parallel to the compressive stress these have increasingly high stress concentrations at their sides. Changes in stress concentrations due to the Poisson's ratio of the matrix are minor, apart from for the intermediate stress at the void sides. Void shape, void separation, and void alignment are critical factors in the concentration of stresses. This suggests a significant departure from strength predictions for porous material that are based solely on scalar values of porosity.

1. Introduction

Natural and manmade voids, cavities, pores, and cracks are ubiquitous in rocks within the Earth's brittle upper crust. Vesicles in volcanic and igneous rocks, pores and vugs in sedimentary rocks, fractures, manmade tunnels, and well bores are all examples of void space at varying scales within rock masses. Increases in bulk rock porosity – defined as the scalar ratio of the void volume to total volume – results in a decrease in the strength of rock (e.g. Dunn et al., 1973). This relationship follows simple trends that can be fitted by an equation describing a line or curve (e.g. Dunn et al., 1973; Kearsley and Wainwright, 2002). However, recent studies of porous material strength that quantified aspects of void topology within the rock, have shown that it is not simply porosity (sensu stricto) that exerts a control on bulk rock strength (Meille et al., 2012; Bubeck et al., 2017): both pore shape and pore orientation have been shown to change the bulk strength of a rock (Bubeck et al., 2017).

Stress concentrations in the material enclosing voids can lead to fracture nucleation. When these fractures propagate and connect voids together this leads to the formation of through-going fractures and eventual bulk failure of the rock mass. Fig. 1a shows two core samples of vesicular basaltic lava from Bubeck et al. (2017) and the fractures that initiated in these cores during uniaxial compression. The stress was applied in a direction that lies parallel to the rulers in the two photos. To conform with coordinates used later in this text we designate this direction as the z-axis. In Fig. 1a) oblate voids (i.e. shortened in the radial length (a) that lies parallel to z, length (a_z)) control the location and propagation of fractures as the core deforms. Fractures meet at the void sides (blue or dark circles) and void poles (red or light circles). These fractures also link voids that are offset with respect to the vertical axis. In Fig. 1b) the radial length a_z of voids is no longer the shortest axis, fractures tend to link the most spherical shaped voids within the core (either from the void side or poles). Fractures in this case align approximately with the core long axis. This figure indicates that both the location and shape of vesicles (voids) within the rock mass influence the pattern of fracturing, and this will be explored in detail in this study.

A number of mathematical formulations exist to evaluate the

* Corresponding author. Aberdeen University, Aberdeen AB24 3UE, UK.
E-mail addresses: davis@gfz-potsdam.de (T. Davis), d.healy@abdn.ac.uk (D. Healy), ab711@leicester.ac.uk (A. Bubeck), rw175@leicester.ac.uk (R. Walker).

http://dx.doi.org/10.1016/j.jsg.2017.07.013
0191-8141/

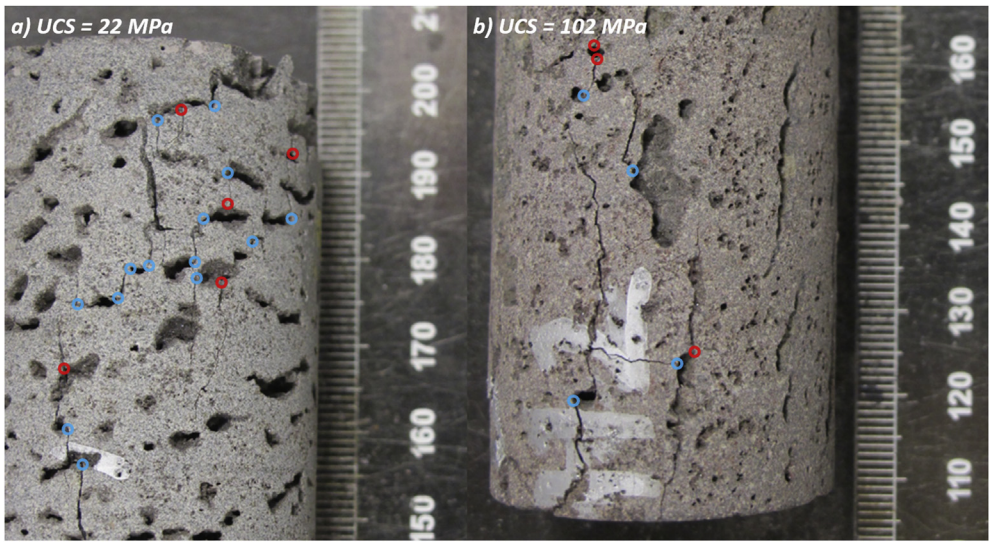

Figure 1. Photographs of basaltic lava core plugs deformed by a vertical uniaxial compressive stress. a) Basaltic lava sample from Bubeck et al. (2017). b) Sample from Bubeck et al. (2017) taken from the same block of material as a) but cored in the orthogonal direction. The sample shown in a) has a lower uniaxial compressive strength (22 MPa) than the sample in b) (102 MPa) (Bubeck et al., 2017). Fractures meeting at void sides are marked with blue or dark circles and those that meet void poles are shown with red or light circles. Scales shown are in millimetres. (For interpretation of the references to colour in this figure legend, the reader is referred to the web version of this article.)

effects of voids on stress concentrations within the surrounding matrix. Within the brittle upper crust deformation is often modelled using the simplified assumption of linear elasticity (Pollard and Fletcher, 2005). Typically these studies are static and two dimensional (2D), but three dimensional (3D) formulations also exist (Kirsch, 1898; Eshelby, 1957; Pollard, 1973; Sammis and Ashby, 1986; Pollard and Segall, 1987; Jaeger et al., 2009; Healy, 2009; Meng et al., 2012). These models offer insight into the behaviour of isolated voids under applied remote stresses. Ling (1948) supplies the analytical solution for interactions of 2D voids in certain positions; stress concentration curves for this solution are supplied in Pilkey and Pilkey (2008). The solution of Eshelby (1957) can also be used to model interacting voids at certain positions with respect to one another (Montheillet, 2003). Numerical studies allow for simulation of failure around voids (e.g. Wang et al., 2013; Huang et al., 2015). These techniques are powerful and can model void interaction and fracture growth in both 2D and 3D respectively. Despite the fundamental nature of the problem however, a comprehensive and systematic analysis of the effects of void shape, interaction, and material properties on stress concentrations in 3D is lacking.

There are a number of theoretical, numerical, and empirical studies into the effects of very low aspect ratio cracks (i.e. Inglis, 1913; Sneddon, 1946). These have infinite stress concentrations at their tips. Our analysis focuses on “fat” voids where the aspect ratio of the shortest/longest diameter of the void is above 0.1. For such analysis, and specifically with respect to rocks and ceramics, closure of void walls can be overlooked. This study applies a 3D semi-analytical method – the displacement discontinuity method (Crouch and Starfield, 1983; Thomas, 1993) – to focus on voids loaded by a uniaxial compressive stress. This method is first compared to the analytical solutions supplied in Jaeger et al. (2009) to show that it accurately produces stress concentrations on the walls of spherical voids. After this, stress concentrations due to non-spherical void shapes and void-void interactions are explored. It is important to note that an engineering stress convention is used here: tension is a positive value; compression is negative. The results of this study can also be used to gain insight into voids that are loaded by a uniaxial tensile stress by simply inverting the sign of the stress concentrations that are supplied.

2. Background

2.1. Theoretical background and terminology

A linear elastic material is one where stress is linearly related to strain, as defined by Hooke's law (e.g., Pollard and Fletcher, 2005). An isotropic elastic material can be described by two elastic material constants that describe how a material deforms under an applied stress, such as Poisson's ratio (ν) and the shear modulus (G). Poisson's ratio is calculated as the axial strain in an axis perpendicular to an applied force divided by the strain measured in the axis parallel to the applied force. This describes the amount a material will extrude in a direction perpendicular to the applied compression. G, a constant that relates shear stress to shear strain, has no effect on stress concentrations around voids where stress is the boundary condition. This constant is therefore irrelevant to this study.

Traction plays a central role in the mathematical description of a void. A traction is a measure of how force is transferred across a surface within a material. It is measured at a point along a boundary in the material and measures the force per unit area imparted due to the material on one side of this boundary surface as its force is transferred into the material on the other side (Pollard and Fletcher, 2005). Mathematical descriptions of stresses due to the presence of a void state that the void edge is traction free, i.e. no normal traction (t_n) or shear traction (t_s) can exist on the void boundary. This is because there is no material within the void to impose the equal and opposite forces to those imposed from the material of the surrounding matrix lying along the void edge. Stresses can exist at the void edge, but not shear or normal tractions.

The equations for analytical solutions that supply stresses around isolated voids under uniaxial stress provide the following insights:

- The greatest tensile and compressive stress concentrations due to a void must always exist at its edge (Pollard and Fletcher, 2005).

- Stress concentrations are independent of void size (Jaeger et al., 2009).
- The void edge acts as a free surface. t_n & t_s cannot exist at this surface so one principal stress on the edge must be zero. A normal stress that lies parallel to the void edge is the only stress at this boundary, this is referred to as hoop or tangential stresses.

Before introducing analytical formulas for stresses around cavities, the stress tensor notation and coordinates used in this study are outlined. Stresses σ_{yy} and σ_{zz} are normal components of stress that align with the Cartesian axes (Pollard and Fletcher, 2005). In this study these stress components define the far field driving stress that is used to compress the void in the y (2D) or z (3D) axis; see Fig. 2. Tensors that define stresses in cylindrical coordinates are used to evaluate stress on the boundary of 2D voids. Here θ in 2D is the angle measured away from the y-axis. $\sigma_{\theta\theta}$ is the normal component of the cylindrical stress tensor and lies in a direction tangential to the radial direction, i.e. tracing the void boundary (Jaeger et al., 2009). Spherical coordinates are used to evaluate hoop stresses at the boundary of a 3D void. In spherical coordinates, tensor component $\sigma_{\Phi\Phi}$ is tangential to the radial direction and has an additional constraint that it points down dip. $\sigma_{\theta\theta}$ is perpendicular to this and thus lies in the strike direction of the voids wall, provided Φ is the angle measured away from the z-axis, see Fig. 2. Principal stresses σ_1, σ_2 and σ_3 are used elsewhere in the study. These define the principal axes of a stress ellipsoid, here the maximum tensile stress is (σ_1) and maximum compressive stress (σ_3) (Pollard and Fletcher, 2005). In 2D coordinates σ_1 and σ_2 are used to describe the maximum and minimum stresses within the xy-plane. ε_1 and ε_2 are the corresponding principal strains.

Stresses around a 2D void under plane strain conditions can be found using equations known as the Kirsch solution (Kirsch, 1898). The equations are provided in Jaeger et al. (2009) and following the convention stated earlier are as follows:

$$\text{At } L = 1, \quad \sigma_{\theta\theta} = \sigma_{yy}(1 - 2cos2\theta) \tag{1}$$

$$\text{At } L \geq 1, \quad \sigma_{\theta\theta} = \frac{1}{2}(\sigma_{yy})\left[1 + \left(\frac{a}{L}\right)^2\right] - \frac{1}{2}(\sigma_{yy})\left[1 + 3\left(\frac{a}{L}\right)^4\right]cos2\theta \tag{2}$$

Eq. (1) & (2) give the equations for the hoop stress in radial coordinates around a circular void under far field vertical compressive stress (σ_{yy}). xy is the plane of interest in these equations. Eq. (1) represents the hoop stress at the void edge and Eq. (2) represents the stress at any point in the surrounding medium. The stresses in the surrounding material are dependent on the distance of an observation point to the void centre (L), the angle from the y-axis (θ) and the void radius (a). Note that Eq. (1) is independent of void size, validating earlier statements. Eq. (2) shows that 2D radial stress around a void is maximal when $L = 1$, i.e. at the void wall. Each part of the equation contains a division by L so with increased distance from the void edge the hoop stress decreases. The size of the void is (a) in Eq. (2), this value changes the rate at which stress decays with increasing radial distance from the void. This follows a linear relationship, so for a void that is twice the size the stress will decay at half the rate, and so on.

Fig. 3 shows the material displacement and area change around an isolated 2D void. Area change here being the addition of the two infinitesimal principal strains ($\varepsilon_1 + \varepsilon_2$). This shows areas of net area gain exist at the void poles (in red or paler areas) whereas the rest of the medium is contracting (blue or darker shades). The region with the greatest area loss is located at the void side (darker

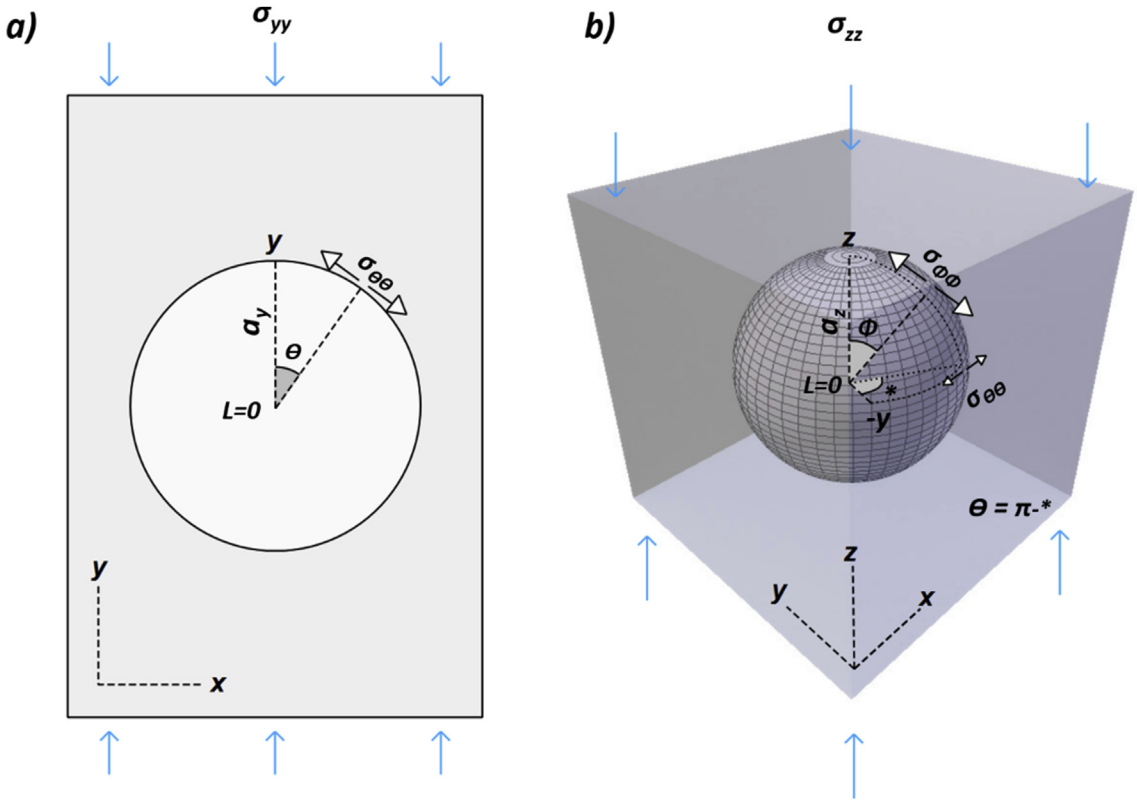

Figure 2. Parameters used in this study, a) 2D and b) 3D. The grey box surrounding the voids represents the isotropic linear elastic host material that extends to infinity and does not represent a boundary.

shades). Note maximum warping of the material as the void edge is approached. For visual effect the deformation shown in Fig. 3 is vastly exaggerated compared to what would be expected for a typical rock. If the matrix here had a Young's modulus of 500 GPa and the driving stress was 0.1 GPa then the displacement shown here is 80 times larger than that of such a rock.

The hoop stresses around the walls of a 3D spherical void under remote compressive stress σ_{zz} are also provided in Jaeger et al. (2009). These two equations provide similar insights to Eq. (1).

$$\sigma_{\Phi\Phi} = \left(\frac{27-15\nu}{2(7-5\nu)} - \frac{15}{(7-5\nu)}\cos^2\Phi\right)\sigma_{zz} \tag{3}$$

$$\sigma_{\theta\theta} = \left(\frac{-3(1-5\nu)}{2(7-5\nu)} - \frac{15\nu}{(7-5\nu)}\cos^2\Phi\right)\sigma_{zz} \tag{4}$$

In these equations the angle measured away from the z-axis is Φ. The vertical far field driving stress is σ_{zz}.

The derivations of Eq. (1)–(4) are detailed in Jaeger et al. (2009). These equations show that the uniaxial compressive driving stress D (σ_{yy} in 2D and σ_{zz} in 3D) induces tensile stress concentrations at the void poles and compressive stress concentrations at the void sides. The maximum tensile and compressive hoop stress concentration factors due to driving stress D are shown in Fig. 4. As no shear and normal stress can exist at the void wall the hoop stresses ($\sigma_{\Phi\Phi}$ & $\sigma_{\theta\theta}$) from Eq. (1)–(4) are also the nonzero principal stresses in this figure. Unlike the 2D plane strain solution the 3D solution is dependent on Poisson's ratio (ν), a material property of the surrounding matrix. When ν is not 0.2 σ_1 or σ_2 at the void equator marked * in Fig. 4b will take positive or negative values as $\sigma_{\theta\theta}$ is no longer 0.

The stress concentrations shown diagrammatically in Fig. 4 and detailed in Eq. (1)–(4) can be used to propose some testable predictions that give some insight into the mechanics underlying void failure:

- Cracks will initiate at void walls where stress concentrations are maximal.
- Tensile cracking will initiate at the poles of compressed voids.
- Shear failure will occur at the side of compressed voids.

These predictions are confirmed by the analogue experiment of Lajtai (1971), and a photo from this study is shown in Fig. 5. This figure shows tensile cracking at the void poles (1) and then shear failure occurring at its sides (fractures labelled 2a and 2b). Additional fractures labelled (3) form under even higher compressive stresses.

Assuming a typical composite Mohr-Coulomb failure envelope, as shown in Fig. 6, we can cast two equations that predict the uniaxial compressive driving stress (D) required for failure around a void due to the tensile and compressive hoop stress concentrations at its wall. For tensile stress concentrations this is expressed as:

$$D = -\frac{T_u}{|\sigma_{conc}|} \tag{5}$$

And for compressive stress at the void sides:

$$D = -\frac{2C\cos\varphi}{|\sigma_{conc}|(1-\sin\varphi)} \tag{6}$$

In Eq. (5) & (6) the cohesive strength (C), tensile strength (T_u), and the angle of internal friction (φ) are properties describing how

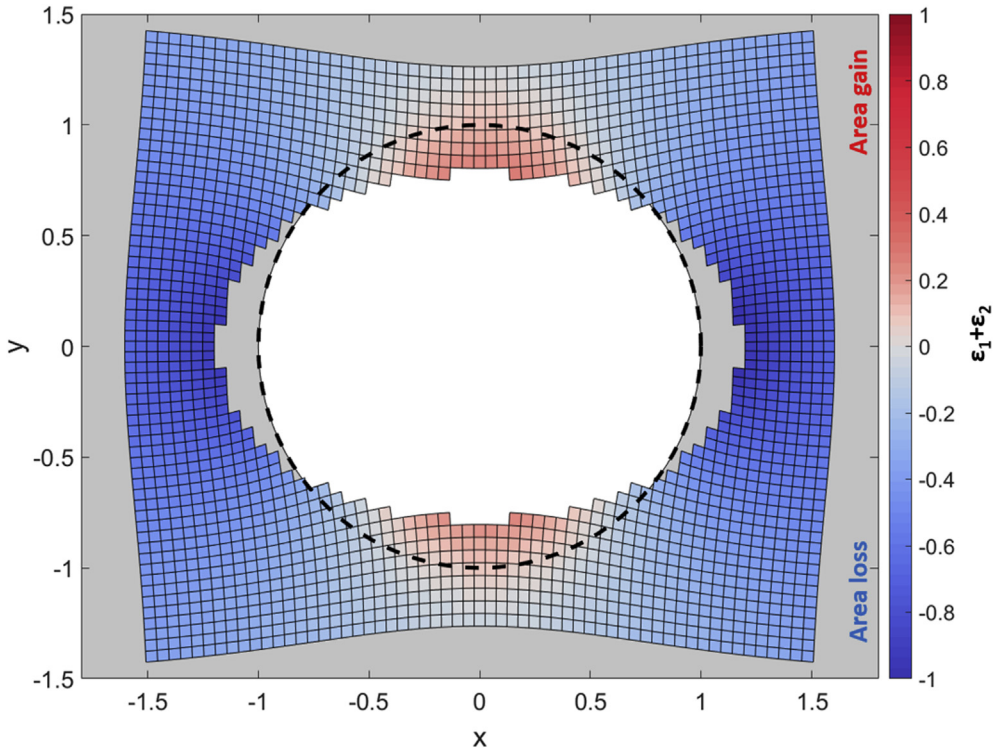

Figure 3. Map of displacement and area change ($\varepsilon_1 + \varepsilon_2$) of material around a 2D circular void under uniaxial vertical compression, plane strain conditions. The void has been modelled within an infinite medium; the sheet like appearance of the grid is shown for visual effect. This was modelled using the numerical method TWODD with a void boundary composed of 300 elements (Crouch and Starfield, 1983). The white circle and its black dotted outline shows the voids original size and shape. Values are scaled so the area change at the side of a circular void is −1. The grid in the figure was originally uniform squares of length 0.05 × 0.05 in xy before deformation. The relative warping of the material in this figure gives an impression of both strain and stress magnitude and direction within the elastic material surrounding the void.

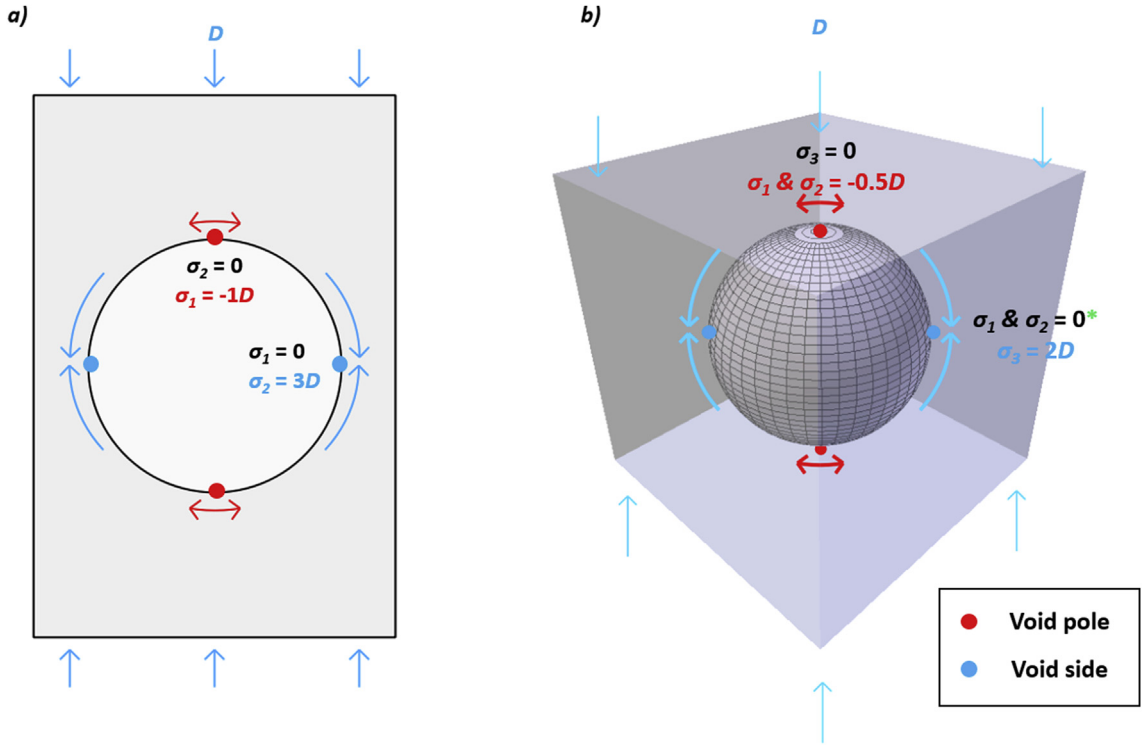

Figure 4. Schematic diagrams of hoop stress concentrations around the edges of voids in an infinite elastic medium due to uniaxial compressive stress *D*. a) 2D solution from Eq. (1). b) 3D solution from Eq. (3), with a Poisson's ratio (ν) of 0.2. For spherical voids the stress concentration at the void side is the same around the entire equator of the void. Note that the terms 'side' and 'pole' used in this text are locations that are relative to the direction of the uniaxial compressive stress *D*.

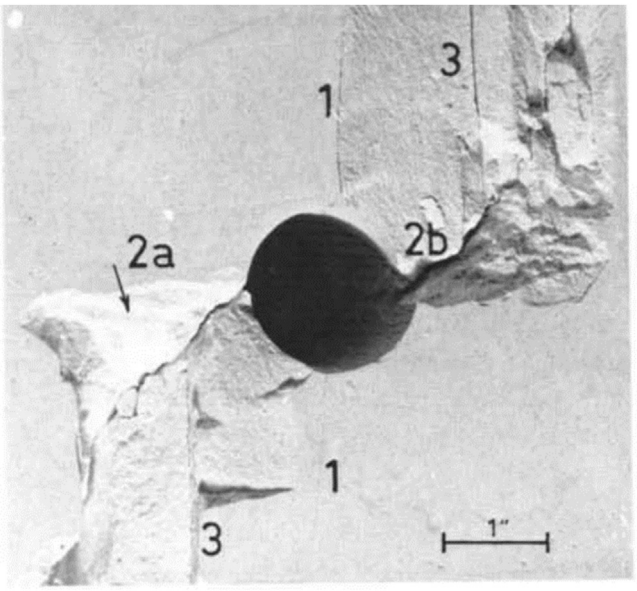

Figure 5. Material failure around a cylindrical void under compression in plaster, fractures labelled in order of initiation. Image is Fig. 14D of Lajtai (1971). The scale shown is 1 inch (2.54 cm).

the material fails. The stress concentration factor (σ_{conc}) is represented as an absolute value as signified by the enclosing vertical bars. If both the material failure criteria are known for a rock type along with the stress concentrations at the void edge then the driving stresses found using Eq. (5) or Eq. (6) can be used to assess the potential sequence of void failure as the driving stress (D) increases.

A caveat here is that Mohr-Coulomb failure makes a number of assumptions (see e.g., Healy et al., 2015). Failure criterion such as the Mogi-Coulomb criteria may therefore be more suitable for evaluating the proximity to shear failure than Eq. (6): this criterion also requires the intermediate principal stress concentration at the void wall (Al-Ajmi and Zimmerman, 2005). For 2D plane strain conditions the intermediate stress is calculated at any point in the material using, $\nu(\sigma_1 + \sigma_2)$ (Pollard and Fletcher, 2005). For 3D spherical voids the intermediate stress at the void side is only 0 when ν is 0.2, as described in more detail later. Our study evaluates stress concentrations on voids at the locations shown in Fig. 4. It is important to note that the octahedral shear stress concentration used in the Mogi-Coulomb criteria is also maximal at the location we have analysed at the void side.

2.2. Experimental data

Rock deformation experiments can be used to test the predictions provided by the mathematical analysis. Fig. 5 shows the distribution and order of crack initiation surrounding a cylindrical void in plaster which was subjected to vertical uniaxial compression (Lajtai, 1971). The cracks show the same pattern predicted by the mathematical solution of Kirsch (1898) combined with the failure criterion from Eq. (5) & (6). The maximum hoop stresses from Eq. (1) substituted in Eq. (5) & (6) with material properties $T_u = 1.586$ MPa and $\varphi = 10–15°$ indicate that the void shown in Fig. 5 should undergo tensile cracking at its poles before shear failure at its sides (Lajtai, 1971).

Previous studies have shown that there are observable trends between the bulk porosity of a material and its uniaxial compressive strength (UCS) (e.g. Dunn et al., 1973; Al-Harthi et al., 1999; Kearsley and Wainwright, 2002; Sabatakakis et al., 2008; Lian et al., 2011; Meille et al., 2012). These studies show non-linear decreases

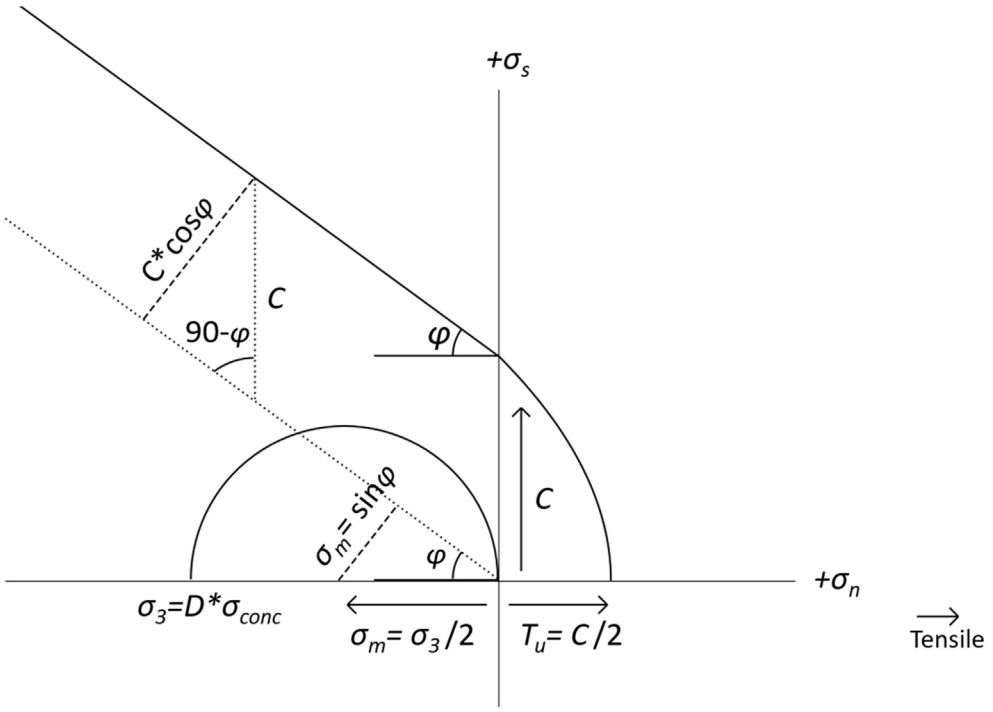

Figure 6. Mohr failure envelope used for Eq. (5) & (6). σ_s & σ_n are the shear and normal stress axes respectively. D is the uniaxial driving stress, C is the materials cohesive strength, T_u its tensile strength and φ its angle of internal friction. σ_3 and σ_m are the most compressive and mean stress. Adapted from Fig. 2 of Bourne and Willemse (2001).

in UCS as bulk porosity is increased. A comparison between pore size, porosity and UCS shows porosity, rather than average pore size, is the dominant parameter affecting UCS (Meille et al., 2012). This is consistent with the insight gained from Eq. (1)–(4). These equations show that the size of a void does not affect the maximum stress concentrations at its edge. Larger voids distribute stress further through the matrix, and therefore may allow fractures to propagate further, but still fail at the same confining stress as smaller voids. The comprehensive failure data of Bubeck et al. (2017) show decreases in bulk rock strength when the smallest diameter of non-spherical voids within a sample is parallel to the remote compressive stress. Notably, Eq. (1)–(4) describe stresses only for perfect cylindrical (2D) or spherical (3D) pores, and do not provide any insight into void shape effects. The effects due to 3D void shape will be explored later in this paper.

3. Methods

Our study uses the displacement discontinuity boundary element method (BEM) which can be used to model both 2D plane strain and 3D problems (Crouch and Starfield, 1983; Thomas, 1993). Our method has been implemented in MATLAB. A single triangular element in the 3D solution describes the effects in the surrounding medium of a constant mirrored movement of the upper and lower faces of the planar triangle within a 3D elastic material (Nikkhoo and Walter, 2015). As voids are manifold (closed contour) surfaces, the basic BEM method used is unstable (Crouch and Starfield, 1983). We have chosen to introduce points inside the void that have no displacement. This is described for the 2D BEM “TWODD” in Crouch and Starfield (1983) and is easily adapted for 3D problems. Once the unknown displacements at each discontinuity on the mesh surface have been found, the sum of stresses at the element mid-points induced by the movement of each face are calculated. These values represent stress changes and require the addition of the driving stress. They are then converted to hoop stresses using each elements normal, strike, and dip directions (Pollard and Fletcher, 2005). As we have found the stresses at the elements mid-points, which are influenced by movement of both sides of each triangle, the resultant hoop stress is multiplied by two. This results in an approximation of the hoop stresses at the outer edge of the voids.

To demonstrate the validity of such a numerical technique, we benchmarked this method to show that our solution accurately produces stresses at a void edge. Fig. 7 shows the analytical (Eq. (3) & (4)) maximum and minimum stresses around a spherical void with different matrix values of Poisson's ratio (ν). The numerical approximation for different values of Poisson's ratio is shown as black dots. This uses a void discretisation of 5120 approximately equilateral triangular faces (see supplementary material). The maximum error for the points shown in Fig. 7 have been calculated. This is greatest for the tensile stress at the void poles when ν is 0.5, here the error is 2% of the driving stress. This shows both the method and the sampling used provides results of acceptable accuracy. This sampling is used in all numerical plots later in this text.

4. Results

4.1. Effect of varying the matrix Poisson's ratio

For 3D problems, the Poisson's ratio of the matrix affects the stress concentrations around the sides of spherical voids Eq. (3) & (4). Maximum tensile and compressive stress concentrations for the void poles and sides are plotted in Fig. 7 as a function of Poisson's ratio. Higher values of ν cause greater stress concentrations at both the void poles and for the compressive stress at the void sides. The tensile stress concentration can be a factor of 5 times higher due to ν. When ν is below 0.2, the stress $\sigma_{\theta\theta}$ at the void side is tensile. For values of ν below 0.2 Eq. (6) is invalid as it assumes there is no tensile stress concentration at this point on the void wall.

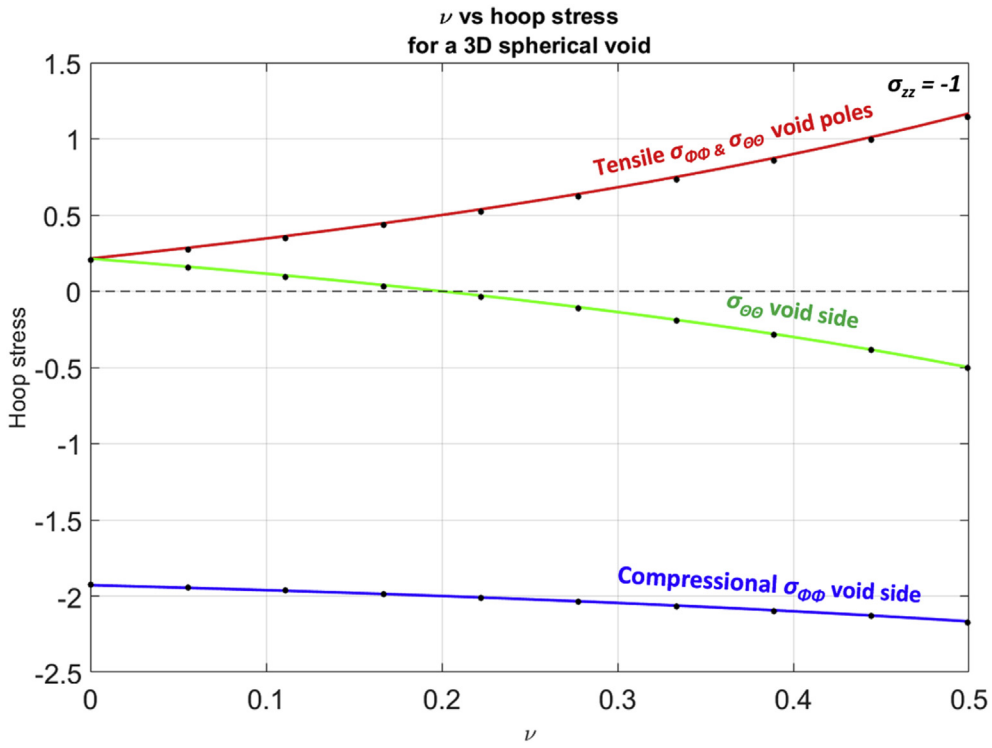

Figure 7. Graph showing the relation between Poisson's ratio (ν) and the hoop stress concentrations on the walls of a spherical void. Lines in this figure are plotted using the analytical solution, Eq. (3) & (4). Dots show the results of the numerical solution detailed in section 3.

4.2. Effect of void shape

It is well established in linear elastic fracture mechanics that cracks loaded by a tensile stress have infinite stress concentrations at their tips. Inglis (1913) showed this effect by approximating a crack as an elliptical 2D void which was flattened in one axis. The following equations describe the stress concentrations at the 'tip' of this void as it is thinned.

$$\rho = \frac{a_y 2}{a_x} \tag{7}$$

$$\sigma_{conc} = \sigma_{yy}\left(1 + 2\sqrt{\frac{a_x}{\rho}}\right) \tag{8}$$

where a_x and a_y are semi-axis or radial lengths of the elliptical void in the x and y directions, respectively: ρ is therefore the radius of curvature of the void wall at the location where the normal to the void wall lies along the x-axis; and σ_{yy} is the driving stress at infinity. As the void thins vertically (decreasing a_y) the radius of the osculating circle at this point decreases (Eq. (7)). This in turn increases the stress concentration exponentially with a linear decrease in the vertical height of the void, (Eq. (8)). Assuming elastic behaviour, flat 2D line cracks therefore have infinite stress concentrations as the radius of curvature at the crack tip tends towards 0. Displacement and area change are shown for two 2D elliptical voids in Fig. 8. It can be seen that the oblate void of Fig. 8a has greater decreases in material area at its sides than both Figs. 3 and 8b, leading to higher stress concentrations.

A similar trend is observed in three-dimensions (Fig. 9). Fig. 9 shows prolate and oblate shaped voids where the radial length in the z-axis is changed (a_z). This length lies parallel to the vertical compressive stress (σ_{zz}). This figure shows voids have increasingly high compressive stress concentrations at their sides as a_z is shortened and the voids flatten in the z-axis.

The void side compressive stress concentration in Fig. 9 increases exponentially as the radial length a_z is decreased linearly, whereas the tensile concentration at the void poles is approximately constant. Poisson's ratio ν has a minor effect on the maximum tensile and compressive concentrations when compared with the effects due to void shape. Only for the intermediate stress at the void side does the value of ν significantly change the stress concentrations, and this is increasingly apparent for flatter, more oblate voids. For prolate and oblate shaped voids, flattened or stretched along the x-axis (radius a_x), i.e. perpendicular to the driving stress, different trends are observed (Fig. 10).

Unlike the stress concentrations shown in Fig. 9, the maximal stress concentrations for voids lengthened or flattened in the x-axis decrease with decreasing void aperture. This is true for both oblate and prolate voids. For increasingly long prolate voids lying along the x-axis, the compressive and tensile stress concentrations trend towards the concentrations observed for 2D cylindrical voids, (Eq. (1) & Fig. 4). As for the trends shown in Fig. 9, Poisson's ratio has a minor effect compared to changes due to the void aperture. Additional data for the compressional stress at the point where the void equator has the greatest curvature are supplied in the supplementary material.

4.3. Effect of void interaction

We now explore the stress concentrations due to interaction of closed 3D voids. This problem has been touched upon in previous studies in 2D. Stress concentrations at the sides of two voids aligned parallel and perpendicular to the driving stress are described in Ling (1948). This showed that for interactions orientated perpendicular to the driving stress, the greatest compressive

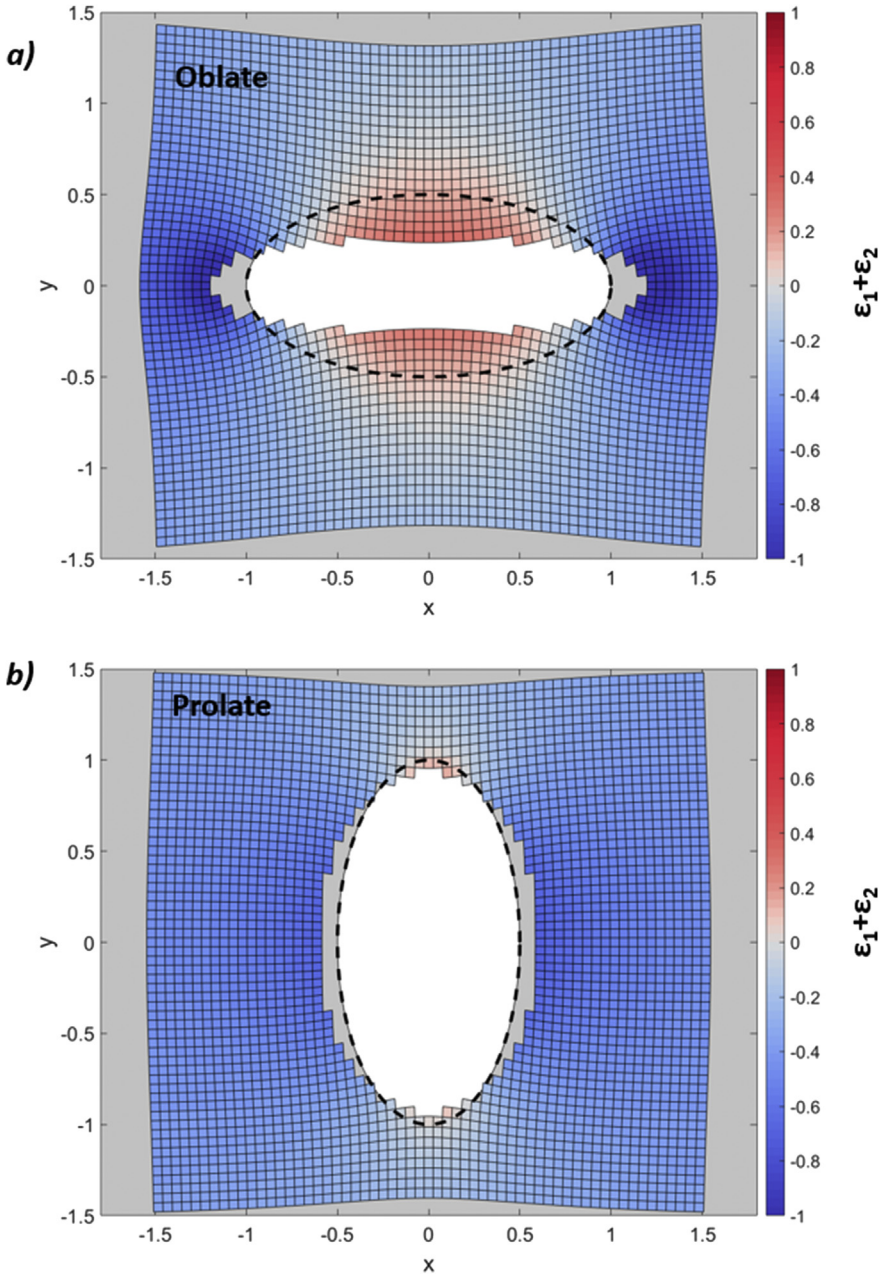

Figure 8. Map of displacement and area change ($\varepsilon_1 + \varepsilon_2$) around 2D voids with different axial ratios. This diagram uses the same numerical method, parameters and colour scale as those described for Fig. 3. The size of squares on the grid before deformation was 0.05 × 0.05 in *xy*.

stress at the void side increases exponentially as the void-void distance decreases; the stress concentration increases as voids get closer together. Somewhat counter intuitively, two voids aligned with the principal stress dampen the stress concentrations at the void side, leading to stress concentrations that are less than those for a single void. A visualisation of interacting voids aligned perpendicular to the driving stress is shown in Fig. 11. This shows increased warping and 2D area change at the void side as the void separation decreases. Comparing Fig. 11a and b there is greater vertical contraction of material between the two voids when these are closer together.

We now explore the effect of void interaction in 3D, looking at both the void side and void polar stresses due to void arrangements that are parallel, inclined (45°) and perpendicular to the driving stress. Different proximities and orientations with respect to the compressive driving stress are plotted, along with the void shape. Note that Figs. 12 and 13 are scaled differently in the *y*-axis. Point *I* in these figures represents the tensile and compressive stress concentration at the side of an isolated spherical void.

Firstly, we will review the interaction of spherical voids under compressive stress σ_{zz} and the effects of void proximity on tensile and compressive stress concentrations, as shown in Figs 12 and 13.

- Vertical interaction reduces both tensile and compressive stress concentrations.
- Diagonal and horizontal interaction increases the void polar stresses and stress concentrations at the void side.

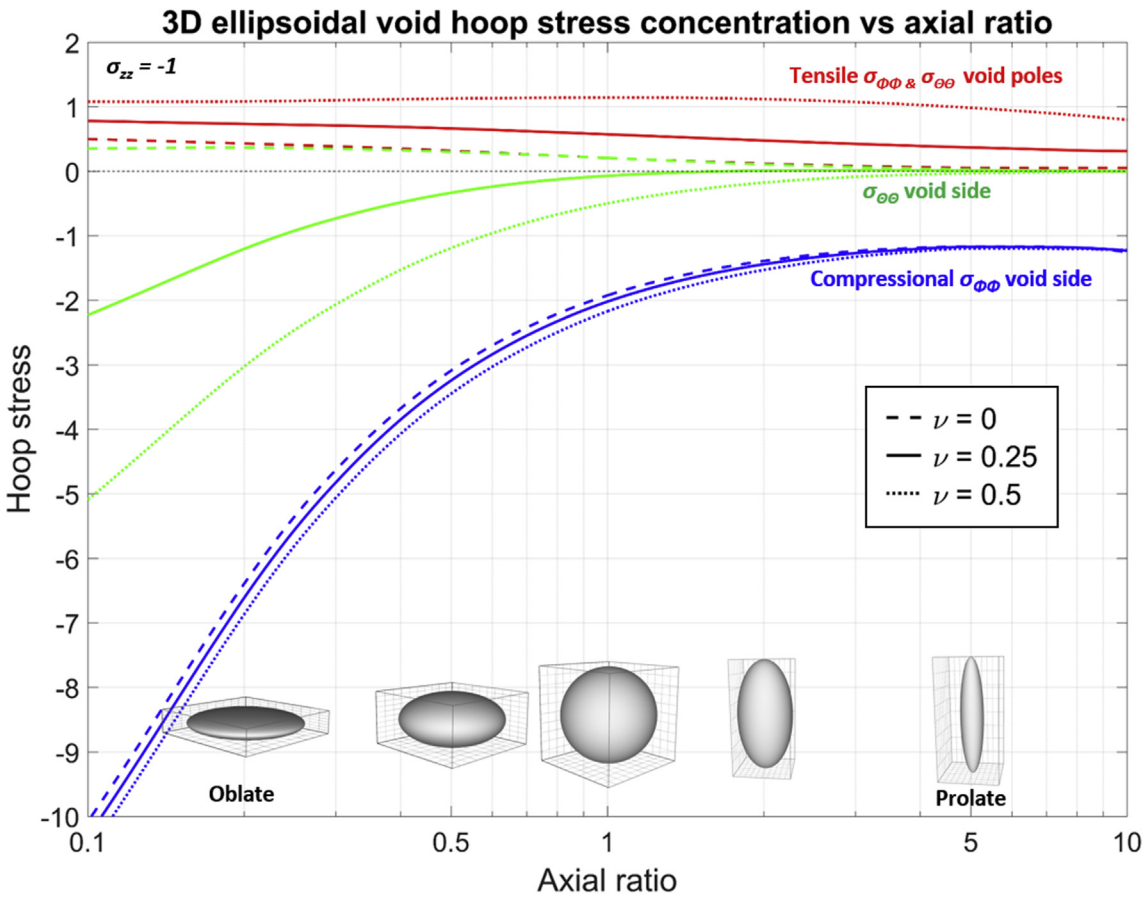

Figure 9. Graph showing 3D ellipsoidal void wall hoop stress concentration vs axial ratio. Axial ratio is calculated as: a_z/a_x and the concentrations shown are due to vertical compressive stress σ_{zz}. Voids shown along base of this graph sit at their respective axial ratios. Plots created using the numerical BEM solution.

- Inclined interaction greatly increases the tensile stress concentration at the void poles.
- Horizontal interaction at close proximities has a pronounced effect compared to other interactions. This greatly increases the compressive stress concentration at the void side when the void walls are separated by a distance smaller than the voids radial length (a).

When different void aspect ratios are introduced, the stress concentrations due to interaction show different trends. A 50% reduction in one axis of the void can reduce or increase the stress concentration by an amount that is far greater than that due to interaction, unless void-void distances are very small. Decreasing the void axis a_z increases the background stress concentration due to axial ratio effects explored earlier (Fig. 9); this reduction also increases the relative gradients of the stress concentrations as the voids are brought into closer proximity. This trend is not observed when axis a_x is reduced in size. Interaction distances of six times the longest void radius have stress concentrations similar to that of an isolated void, as shown in Figs. 12 and 13. The numerical analysis used in the research is unstable when voids are touching, and therefore the data shown in Figs. 12 and 13 stop when void walls are separated by a distance L/a of less than 0.2. All five modelled void shapes show that horizontal interaction may follow the trend observed in 2D where the compressive stress reaches infinite levels for cases where the voids are nearly touching. The intermediate stresses are not shown in Figs. 12 and 13, but these are included in the supplementary material.

5. Discussion

5.1. Failure

Poisson's ratio appears to have a moderately small effect on the greatest compressive and tensile stress concentrations, whereas the intermediate stress at the void side is strongly influenced by this property, (Figs. 9 and 10). Shear failure criteria that are dependent on the magnitude of the intermediate stress will therefore be sensitive to Poisson's ratio (Al-Ajmi and Zimmerman, 2005). Assuming a Mohr-Coulomb failure criterion that is not sensitive to intermediate stress concentrations, we can substitute values from Fig. 9 into Eq. (5) & (6). For typical rock properties these equations show flatter voids failing in shear at their sides before tensile cracking occurs at the void poles, as observed in the natural samples shown Fig. 1. As for interaction relative to the compressive driving stress σ_{zz} we can state that voids in horizontal and offset arrangements will be closer to both modes of failure, whereas those aligned vertically will be more stable.

It is worth discussing where the predictions of this study fit with the general trend from experimental measurements that uniaxial compressive strength decreases with increases in bulk porosity. Higher porosity materials must have voids in closer packed arrangements. Either due to constant void size where higher porosity means voids will be packed closer together or due to increases in void size leading to decreased pore-pore distances. This will broadly lead to higher stress concentrations and therefore failure of the material at a lower confining stress. None of the experimental

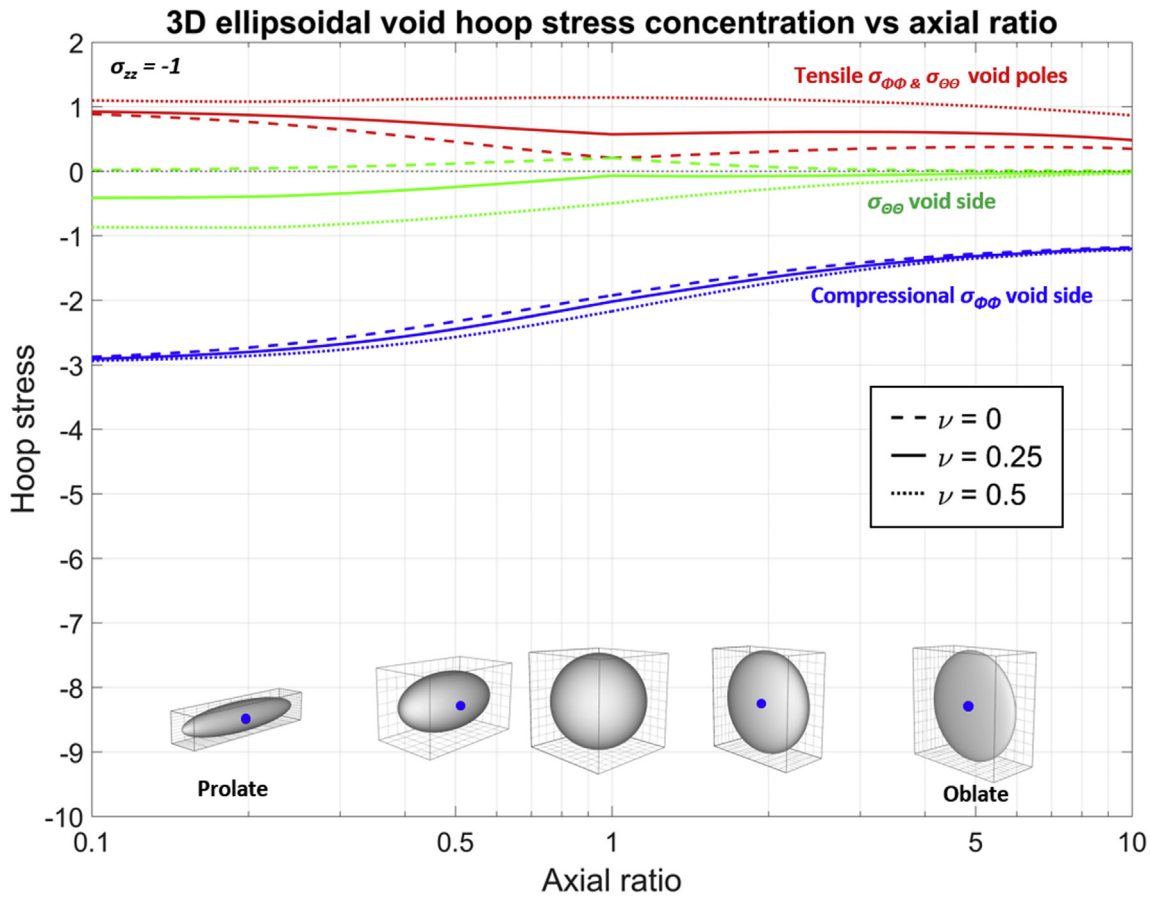

Figure 10. Graph showing 3D ellipsoidal void hoop stress concentration vs axial ratio. Axial ratio is calculated as: a_z/a_x and the concentrations shown are due to vertical compressive stress σ_{zz}. Voids shown along base of graph sit at their respective axial ratios. The void side stresses plotted in this case are at the location of the dot on the voids shown along the base of the diagram. Plots created using the numerical BEM solution.

studies referenced in section 2.2 quantify void topology, i.e. the void-void distances and arrangement with respect to the axis of the driving stress. These studies have only quantified the average porosity, and to a limited extent, pore shape. The results from our analysis suggest there will be a correlation between void topology and the UCS for a given rock sample. A parameter that attempts to describe void topology, size and shape within a rock mass, which is scaled by the trends supplied in this study may correlate better with UCS results than more simplistic parameters such as bulk porosity (Bubeck et al., 2017). Our study has only looked at the effects due to interactions of voids of the same size and shape and additional analysis would benefit from assessing the effects due to a variation of these parameters. The effects of multiple pores are looked at in more detail in the following sections.

5.2. Multi-void interaction

Stress concentrations for 2D voids arranged on a grid are given in Pilkey and Pilkey (2008). This solution is that of plane stress, and shows higher void side stress concentrations for gridded void arrangements that are not aligned with the principal stress, i.e. diamond-shaped patterns if the principal stress is vertical. Pilkey and Pilkey (2008) discuss the stress concentration reductions due to rows of spherical voids aligned with the applied stress. They show that decreases in stress at the void poles due to interaction is approximately 2.5 times the value observed for two interacting spherical cavities. A quantitative analysis of the effects due to gridded arrangements of pores in 3D remains to be explored.

5.3. Triaxial stress states

Interaction and coalescence or voids cracks and fractures in 3D under triaxial stress states is likely to be the general situation within the earth's crust (Healy et al., 2006a, 2006b, 2015). Eq. (3) and eq. (4) can be superposed to approximate the stresses around a void under a triaxial compressive stress state (Jaeger et al., 2009). This can be done for the greatest stress concentrations at the void edge, at the locations shown in Fig. 4. The method of superposition is shown in Fig. 14: the void need not be spherical like shown in this diagram, stress concentrations from Figs. 7, Figs. 9 and 10 as well as additional data in the supplementary material supply the stress at the point shown due to different parameters.

Superposing the values from Fig. 4 for a 3D void in a matrix where $\nu = 0.2$ gives the stress concentrations at the walls of a void due to uniform triaxial compression as: $\sigma_{\Phi\Phi} = -1.5$ and $\sigma_{\theta\theta} = -1.5$. This is a smaller compressive stress concentration on the void wall than that due to a uniaxial compressive stress and no tensile stress exists at any point on the void wall.

5.4. Coalescence

Our study has focussed on the elastic deformation prior to brittle fracturing. The directions in which fractures propagate depends primarily on the stress field of the matrix through which they are propagating (Pollard and Fletcher, 2005). The least compressive stress in the matrix between the two voids tends to lie in orientations approximately perpendicular to the walls of the

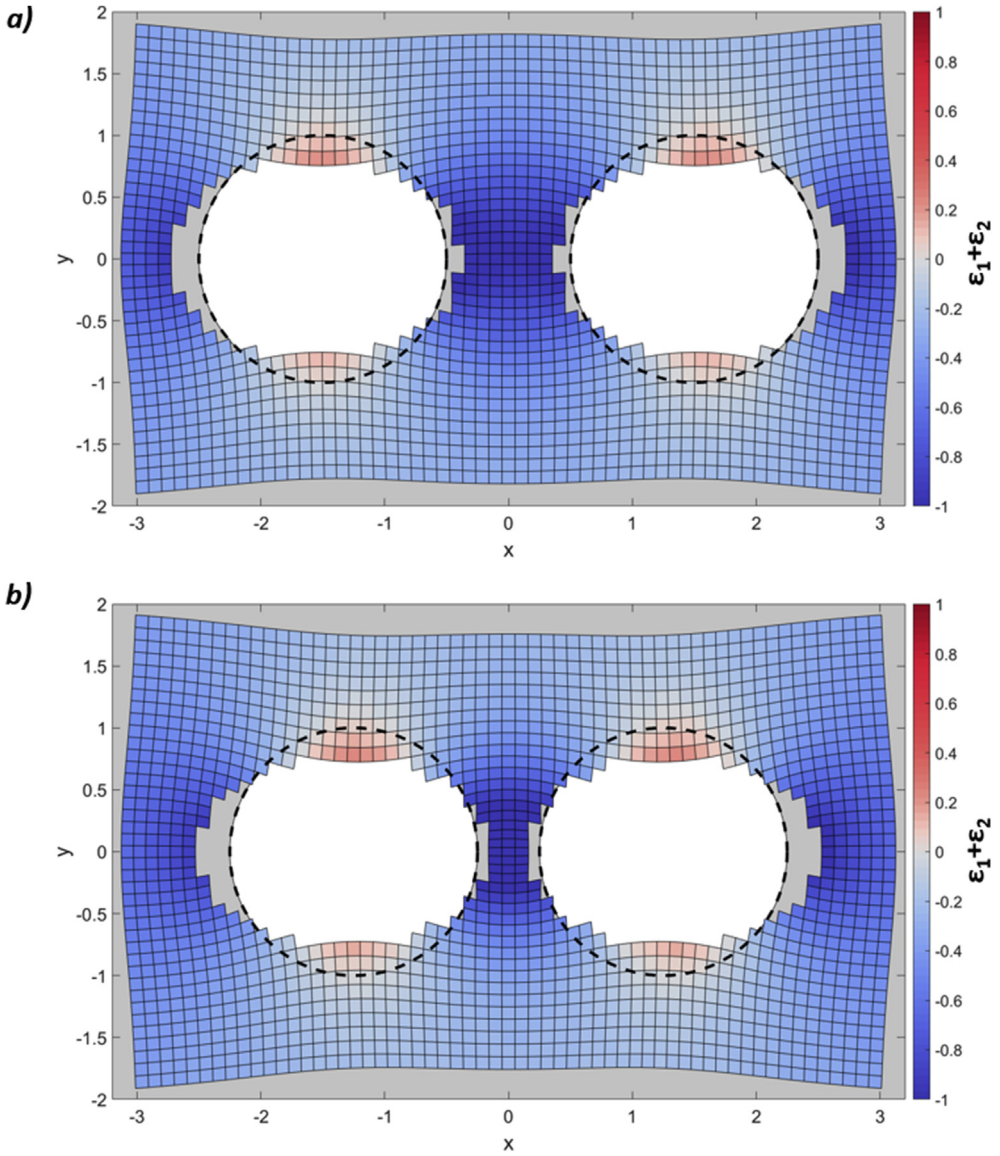

Figure 11. Map of displacement and area change due to 2D circular void interaction. If a is the radius and L the distance between the void mid-points then for a) $a/L = 3$ & b) $a/L = 2.5$. Deformation of a spherical void is shown in Fig. 3 which uses the numerical method, parameters and colour scale. The size of squares on the grid before deformation was 0.1×0.1 in xy.

voids, apart from at the void poles. At the void poles there is a small zone of area gain (Fig. 3); only in this zone do the least compressive stresses approximately lie parallel with the void wall. If fractures propagate along the direction of the most compressive stress, then tensile fractures initiating from void poles are unlikely to link two voids together unless they are in arrangements that are close to vertical alignment. This is supported by findings from 2D numerical models of voids under plane strain conditions, which show that tensile fractures will only propagate from the void poles and connect with neighbouring voids when they are aligned vertically and parallel to the axis of applied stress (Wang et al., 2013).

Shear cracks initiating from void sides do not directly align with the direction of the most compressive stress (observed fractures in Fig. 5). Instead these grow at orientations angled with respect to the most compressive stress, where this angle is presumably related to the angle of internal friction of the material (Pollard and Fletcher, 2005). For an isolated void when the shear crack reaches a certain distance from the void edge this will either arrest or turn to propagate parallel with the driving stress direction. A crack will continue to propagate provided there is enough energy to keep cracking the rock and extending the fractures tip (Martel, 2017). The alignment of the fracture with the driving stress direction can be gradual, producing curved fractures or more abrupt 'wing crack' fractures like those labelled (3) in Fig. 5 (Martel, 1997).

Lajtai and Lajtai (1975) model arrays of voids under compression, they show some examples of shear fractures and how these connect arrays of cylindrical voids in plaster. Voids arranged in patterns close to parallel with the driving stress create shear fractures that change mode into tensile fractures at certain distances from the void. These tensile fractures eventually link the two voids. When voids are in arrangements that are at greater angles from the driving stress these appear to link purely through intersection of shear cracks emanating from the walls of both voids. Fig. 15 of Huang et al. (2015) clearly shows that shear cracks initiating from the void sides in 3D control the arrangement of the final fracture network.

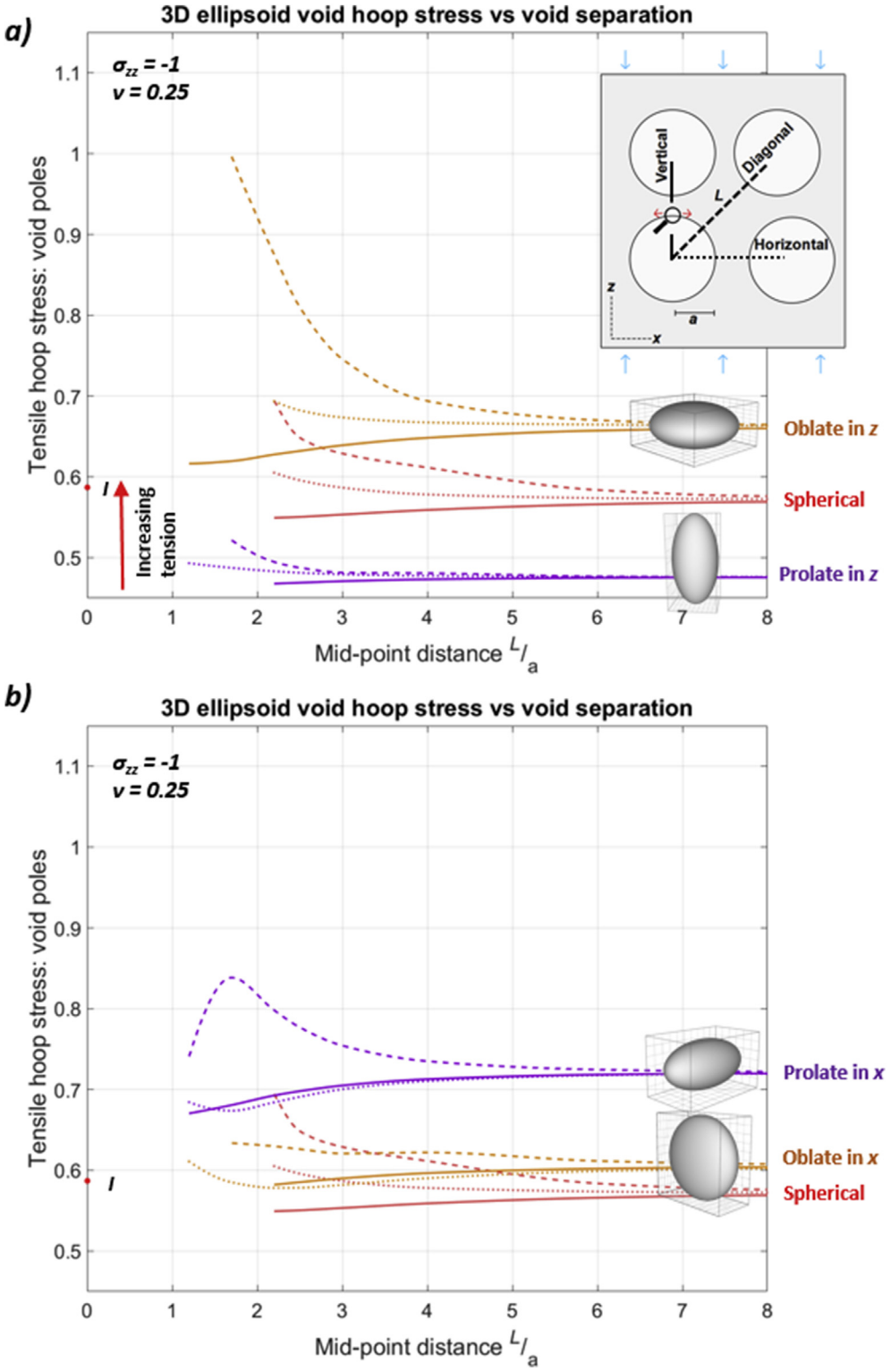

Figure 12. Graphs showing 3D ellipsoidal void tensile hoop stress vs the void separation. Void polar tensile hoop stress concentration vs a) Voids changed in radial length a_z and b) Voids changed in radial length a_x. Axial ratios used are ratios of 1:2. The legend in the upper right summarises the line styles used, solid, dashed and dotted are alignments in the vertical, diagonal, and horizontal directions respectively. The longest semi-axis (radius) of the two voids is a and the length separating the mid points is L, which lies within the xz plane. Plots created using the numerical BEM solution, ν was set to 0.25. Minimum separation distance of the void walls is 0.2 L/a.

6. Conclusions

3D voids under vertical uniaxial compression have tensile stress concentrations at their poles and compressive concentrations at their sides. Flatter voids have much greater compressive stress concentrations at their sides than voids that are close to spherical. As the void edge represents a free surface, failure can easily occur with shear cracks forming at the void sides. Depending on shape,

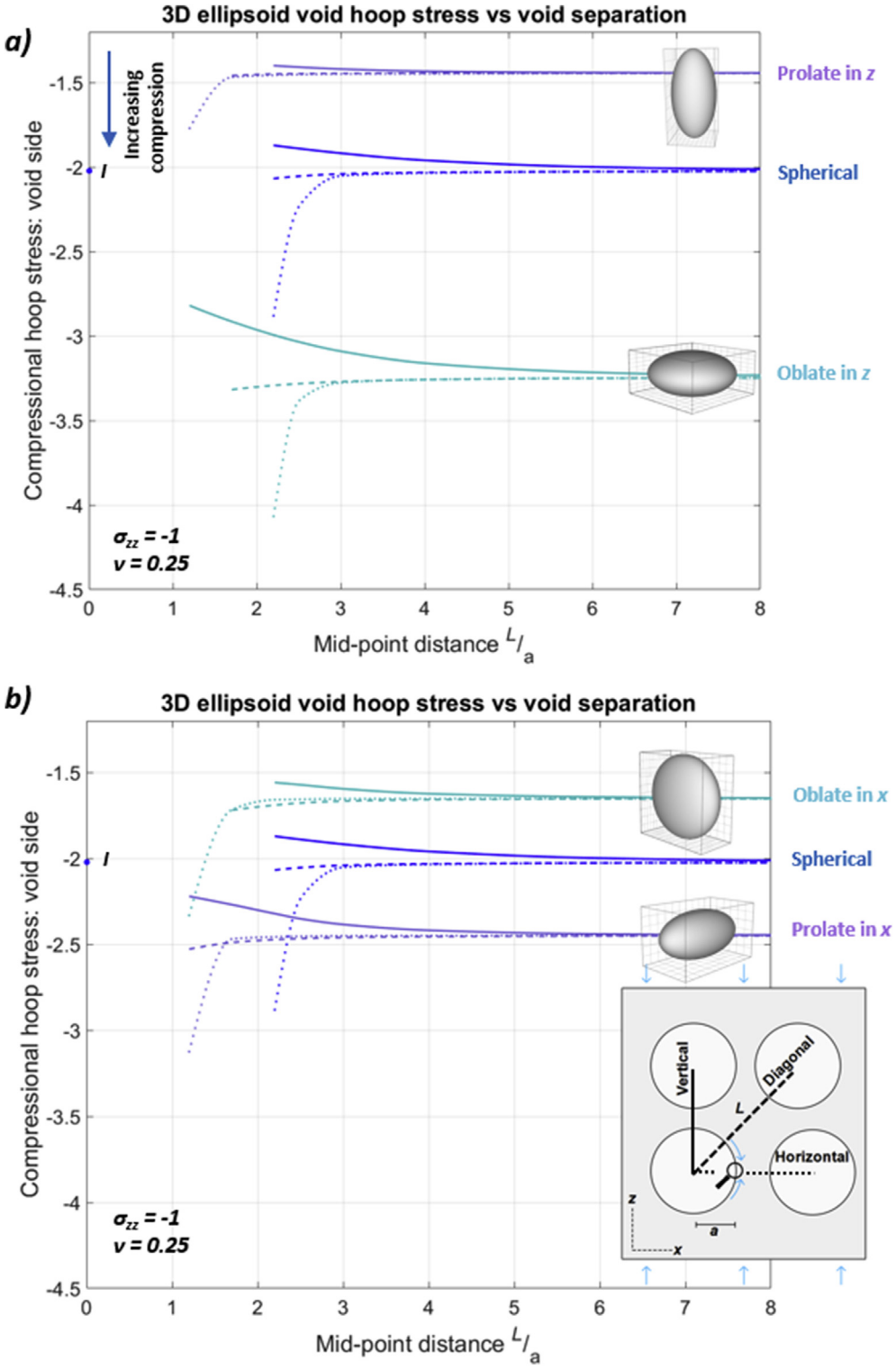

Figure 13. 3D ellipsoidal void compressional hoop stress vs the void separation. Void side compressional hoop stress concentration vs a) Voids changed in radial length a_z and b) Voids changed in radial length a_x. Axial ratios used are ratios of 1:2. The legend in the lower right summarises the line styles used, solid, dashed and dotted are alignments in the vertical, diagonal, and horizontal directions respectively. The longest semi-axis of the two voids is a and the length separating the mid points is L. L lies within the xz plane. Plots created using the numerical BEM solution, ν was set to 0.25. Minimum separation distance of the void walls is 0.2 L/a.

the void may be prone to shear failure at its sides prior to tensile failure at its poles. When voids interact, higher tensile and compressive stress concentrations are observed for void configurations that are aligned perpendicular or inclined to the applied compressive stress direction. Poisson's ratio has a negligible effect on the maximum and minimum stress concentrations especially when compared to the axial ratio of the void, however it does greatly affect the intermediate stress at the voids side.

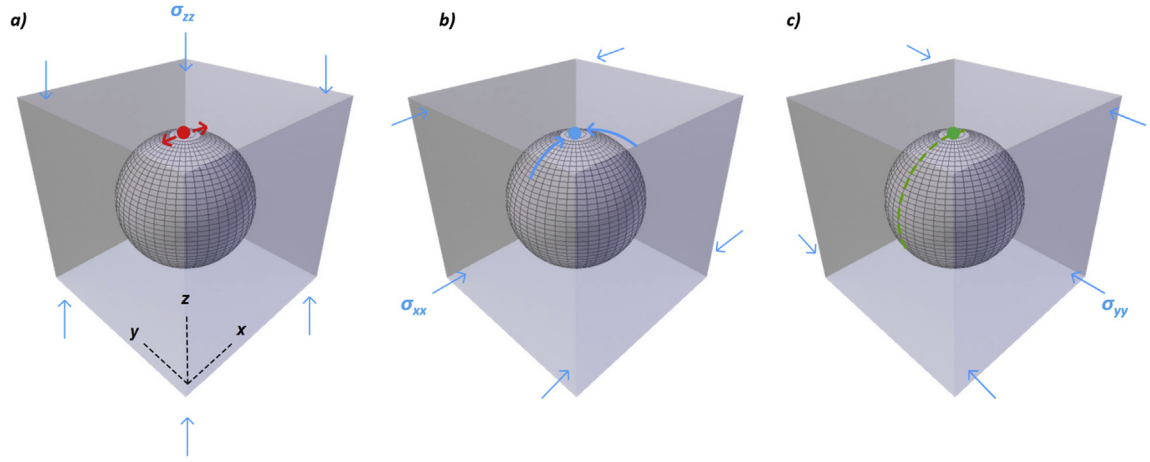

Figure 14. Summary diagram that shows how to superpose the greatest stress concentrations at the edge of a void. This can be used to approximate stress concentrations due to 3D triaxial stress states (Jaeger et al., 2009). The diagram shows the components that are summed to estimate triaxial stress concentrations at the marked point on the void wall, this summation supplies the concentration directed along the *x*-axis. The driving stresses and need not be equal in each direction. The stresses concentrations due to the remote driving stresses σ_{xx}, σ_{yy} and σ_{zz} at the point shown in a) b) and c) are simply summed.

In summary, we have quantified how certain parameters control porous rock strength. Under a compressive stress a weaker rock will have in approximate order of significance:

- Flatter voids, shortened in the axis parallel with the driving stress (most significant).
- Closely packed voids in arrangements offset with respect to the driving stress.
- A matrix with a higher Poisson's ratio (least significant).

This study has provided a quantitative evaluation of the precursors to failure within a 3D elastic porous medium. The results indicate that a parameter describing the topology of void space within a rock mass may provide a more robust first order estimate of rock strength.

Funding

This work forms part of a NERC New Investigator award for DH (NE/I001743/1), which is gratefully acknowledged.

Acknowledgments

The authors would like to acknowledge the reviewers, Elizabeth Ritz and Phillip Resor. Their reviews were very constructive, both helping to improve the manuscripts consistency and highlighting a number of errors in the initial submission. The authors would also like to thank Lydia Jagger's keen eye and patience, she helped greatly in removing a number of grammatical errors from the initial draft.

Appendix A. Supplementary data

Supplementary data related to this article can be found at http://dx.doi.org/10.1016/j.jsg.2017.07.013.

References

Al-Ajmi, A.M., Zimmerman, R.W., 2005. Relation between the Mogi and the Coulomb failure criteria. Int. J. Rock Mech. Min. Sci. 42 (3), 431–439.
Al-Harthi, A.A., Al-Amri, R.M., Shehata, W.M., 1999. The porosity and engineering properties of vesicular basalt in Saudi Arabia. Eng. Geol. 54 (3), 313–320.
Bourne, S.J., Willemse, E.J., 2001. Elastic stress control on the pattern of tensile fracturing around a small fault network at Nash Point, UK. J. Struct. Geol. 23 (11), 1753–1770.
Bubeck, A., Walker, R.J., Healy, D., Dobbs, M., Holwell, D.A., 2017. Pore geometry as a control on rock strength. Earth Planet. Sci. Lett. 457, 38–48.
Crouch, S.L., Starfield, A.M., 1983. Boundary Element Methods in Solid Mechanics. Allen and Unwin.
Dunn, D.E., LaFountain, L.J., Jackson, R.E., 1973. Porosity dependence and mechanism of brittle fracture in sandstones. J. Geophys. Res. 78 (14), 2403–2417.
Eshelby, J.D., 1957, August. The determination of the elastic field of an ellipsoidal inclusion, and related problems. Proc. R. Soc. Lond. A: Math. Phys. Eng. Sci. 241 (1226), 376–396. The Royal Society.
Healy, D., 2009. Elastic field in 3D due to a spheroidal inclusion—MATLAB™ code for Eshelby's solution. Comput. Geosci. 35 (10), 2170–2173.
Healy, D., Jones, R.R., Holdsworth, R.E., 2006a. Three-dimensional brittle shear fracturing by tensile crack interaction. Nature 439 (7072), 64–67.
Healy, D., Jones, R.R., Holdsworth, R.E., 2006b. New insights into the development of brittle shear fractures from a 3-D numerical model of microcrack interaction. Earth Planet. Sci. Lett. 249 (1), 14–28.
Healy, D., Blenkinsop, T.G., Timms, N.E., Meredith, P.G., Mitchell, T.M., Cooke, M.L., 2015. Polymodal faulting: time for a new angle on shear failure. J. Struct. Geol. 80, 57–71.
Huang, Y., Yang, Z., Ren, W., Liu, G., Zhang, C., 2015. 3D meso-scale fracture modelling and validation of concrete based on in-situ X-ray computed tomography images using damage plasticity model. Int. J. Solids Struct. 67, 340–352.
Inglis, C., 1913. Stresses in a cracked plate due to the presence of cracks and sharp corners. Trans. Nav. Archit. Lond. 60, 213.
Jaeger, J.C., Cook, N.G., Zimmerman, R., 2009. Fundamentals of Rock Mechanics. John Wiley & Sons.
Kearsley, E.P., Wainwright, P.J., 2002. The effect of porosity on the strength of foamed concrete. Cem. Concr. Res. 32 (2), 233–239.
Kirsch, G., 1898. Die theorie der elastizität und die bedürfnisse der festigkeitslehre. Springer.
Lajtai, E.Z., 1971. A theoretical and experimental evaluation of the Griffith theory of brittle fracture. Tectonophysics 11 (2), 129–156.
Lajtai, E.Z., Lajtai, V.N., 1975, April. The collapse of cavities. Int. J. Rock Mech. Min. Sci. Geomech. Abstr. 12 (4), 81–86. Pergamon.
Lian, C., Zhuge, Y., Beecham, S., 2011. The relationship between porosity and strength for porous concrete. Constr. Build. Mater. 25 (11), 4294–4298.
Ling, C.B., 1948. On the stresses in a plate containing two circular holes. J. Appl. Phys. 19 (1), 77–82.
Martel, S.J., 1997. Effects of cohesive zones on small faults and implications for secondary fracturing and fault trace geometry. J. Struct. Geol. 19 (6), 835–847.
Martel, S.J., 2017. Progress in understanding sheeting joints over the past two centuries. J. Struct. Geol. 94, 68–86.
Meille, S., Lombardi, M., Chevalier, J., Montanaro, L., 2012. Mechanical properties of porous ceramics in compression: on the transition between elastic, brittle, and cellular behavior. J. Eur. Ceram. Soc. 32 (15), 3959–3967.
Meng, C., Heltsley, W., Pollard, D.D., 2012. Evaluation of the Eshelby solution for the ellipsoidal inclusion and heterogeneity. Comput. Geosci. 40, 40–48.
Montheillet, F., 2003. The interaction of two spherical gas bubbles in an infinite elastic solid. J. Appl. Mech. 70 (6), 789–798.
Nikkhoo, M., Walter, T.R., 2015. Triangular dislocation: an analytical, artefact-free solution. Geophys. J. Int. 201 (2), 1117–1139.
Pilkey, W.D., Pilkey, D.F., 2008. Peterson's Stress Concentration Factors. John Wiley & Sons.

Pollard, D.D., 1973. Equations for stress and displacement fields around pressurized elliptical holes in elastic solids. J. Int. Assoc. Math. Geol. 5 (1), 11–25.
Pollard, D.D., Fletcher, R.C., 2005. Fundamentals of Structural Geology. Cambridge University Press.
Pollard, D.D., Segall, P., 1987. Theoretical displacements and stresses near fractures in rock: with applications to faults, joints, veins, dikes, and solution surfaces. Fract. Mech. Rock 277 (349), 277–349.
Sabatakakis, N., Koukis, G., Tsiambaos, G., Papanakli, S., 2008. Index properties and strength variation controlled by microstructure for sedimentary rocks. Eng. Geol. 97 (1), 80–90.
Sammis, C.G., Ashby, M.F., 1986. The failure of brittle porous solids under compressive stress states. Acta Metall. 34 (3), 511–526.
Sneddon, I., 1946, October. The distribution of stress in the neighbourhood of a crack in an elastic solid. Proc. R. Soc. Lond. A: Math. Phys. Eng. Sci. 187 (1009), 229–260. The Royal Society.
Thomas, A.L., 1993. Poly3D: a Three-dimensional, Polygonal Element, Displacement Discontinuity Boundary Element Computer Program with Applications to Fractures, Faults, and Cavities in the Earth's Crust. Doctoral dissertation. Stanford University.
Wang, S.Y., Sun, L., Yang, C., Yang, S.Q., Tang, C.A., 2013. Numerical study on static and dynamic fracture evolution around rock cavities. J. Rock Mech. Geotechnical Eng. 5 (4), 262–276.